Simulating the Impact Response of Composite Airframe Components

Karen E. Jackson and Justin D. Littell
NASA Langley Research Center
Hampton, VA

Edwin L. Fasanella
National Institute of Aerospace
Hampton, VA

Abstract

In 2010, NASA Langley Research Center obtained residual hardware from the US Army's Survivable Affordable Repairable Airframe Program (SARAP), which consisted of a composite fuselage section that was representative of the center section of a Black Hawk helicopter. The section was fabricated by Sikorsky Aircraft Corporation and was subjected to a vertical drop test in 2008 to evaluate a tilting roof concept to limit the intrusion of overhead mass items, such as the rotor transmission, into the fuselage cabin. As a result of the 2008 test, damage to the hardware was limited primarily to the roof. Consequently, when the post-test article was obtained in 2010, the roof area was removed and the remaining structure was cut into six different types of test specimens including: (1) tension and compression coupons for material property characterization, (2) I-beam sections, (3) T-sections, (4) cruciform sections, (5) a large subfloor section, and (6) a forward framed fuselage section. In 2011, NASA and Sikorsky entered into a cooperative research agreement to study the impact responses of composite airframe structures and to evaluate the capabilities of the explicit transient dynamic finite element code, LS-DYNA®, to simulate these responses including damage initiation and progressive failure. Finite element models of the composite specimens were developed and impact simulations were performed. The properties of the composite material were represented using both a progressive in-plane damage model (Mat 54) and a continuum damage mechanics model (Mat 58) in LS-DYNA. This paper provides test-analysis comparisons of time history responses and the location and type of damage for representative I-beam, T-section, and cruciform section components.

Introduction

In 2008, the Survivable Affordable Repairable Airframe Program (SARAP) Virtual Prototype and Validation (VPV) Program was initiated between Sikorsky Aircraft Corporation and the US Army Aviation Applied Technical Directorate (AATD). The objective of the program was to validate technology advances in design processes, structural efficiency, crashworthiness, materials and manufacturing processes, and reparability of rotorcraft airframe structures. The comprehensive SARAP VPV program [1] included identification, review and evaluation of various design, analysis, material, and manufacturing technologies. As part of this program, a prototype Technology Validation Article (TVA) was constructed, which was representative of the center section of a UH-60 Black Hawk helicopter. Following detailed design, manufacturing, and assembly, a full-scale vertical impact test of the TVA was performed at the Landing and Impact Research (LandIR) facility at NASA Langley Research Center in August 2008. A post-test photograph of the TVA is shown in Figure 1. The purpose of the test was to evaluate the performance of a "tilting roof" concept that was intended to dissipate the kinetic energy of high mass items, such as the rotor transmission, during a crash event [1]. The tilting roof concept required controlled failures of the roof structure with energy absorption obtained through crushing of aluminum tubes.

Post-test inspection of the TVA indicated that damage was primarily limited to the roof area, with little or no damage found in the subfloor, or the forward framed fuselage section. In 2010, NASA Langley obtained the residual SARAP hardware for testing under the NASA Subsonic Rotary Wing (SRW) crashworthiness research program. In May 2011, NASA and Sikorsky

signed a Space Act Agreement [2] allowing cooperation between the two organizations to pursue common research interests, including: composite material and airframe structural testing under dynamic loading; development of accurate and robust material models to predict aircraft structural response using LS-DYNA; and, validation of analytical models through test-analysis correlation.

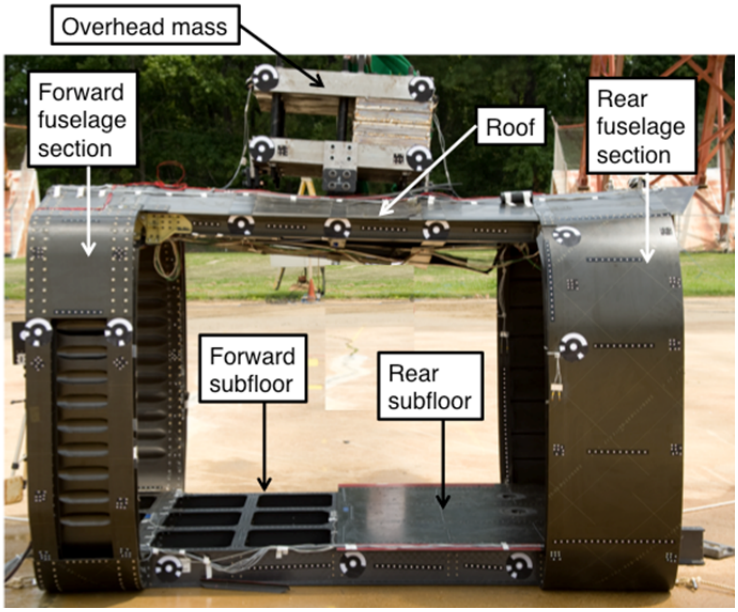

Figure 1. Post-test photograph of the SARAP TVA following the 2008 vertical drop test.

Since its inception in 2006, the SRW crashworthiness research program has focused on improved prediction of rotorcraft crashworthiness, addressing topics such as occupant modeling and injury prediction, multi-terrain impact simulation, model validation studies that focused on probabilistic analysis, and development of system-integrated simulation models [3]. Recently, the research program was refocused to assess current analytical capabilities used to predict crashworthiness of composite airframe structures. Thus, obtaining the SARAP residual hardware was fortuitous and allowed testing of fairly simple coupons, more complex components, and complex built-up airframe structures for the purpose of model validation.

The objective of the joint research program was to assess the capability of LS-DYNA [4, 5], a commercial nonlinear, explicit transient-dynamic finite element code, for predicting damage initiation and progressive failure of composite airframe structures subjected to crash loading. Finite element models were developed to represent each of the test articles and simulations were conducted using LS-DYNA. Specifically, two composite material models were evaluated: MAT_ENHANCED_COMPOSITE_DAMAGE (Mat 54), a progressive failure model that uses the Chang-Chang failure criterion to simulate ply-by-ply failure and property degradation and MAT_LAMINATED_COMPOSITE_FABRIC (Mat 58), a continuum damage mechanics model for representing unidirectional tape and fabric composite materials. Sikorsky provided the material property values for Mat 54, whereas properties for Mat 58 were determined by assessing literature data, by comparing with similar Mat 54 values, and by using a trial and error process in which laminated coupons were simulated under both tensile and compressive loading.

The focus of this paper is to document impact testing and simulation results for the I-beam, T-

section, and cruciform section composite airframe components that were subjected to dynamic compressive loading. Additional information regarding this research program is provided in References 6 and 7.

Experimental Testing

The SARAP residual hardware arrived at NASA in excellent shape. Care was taken to determine the most appropriate use for each portion of the residual hardware to optimize the data generated. Specimens were chosen such that the hardware could be tested from the coupon level all the way to full-scale impact testing. The final layout provided 6 different types of specimens, with a potential for a future seventh specimen. A depiction of the SARAP residual hardware utilization is shown in Figure 2.

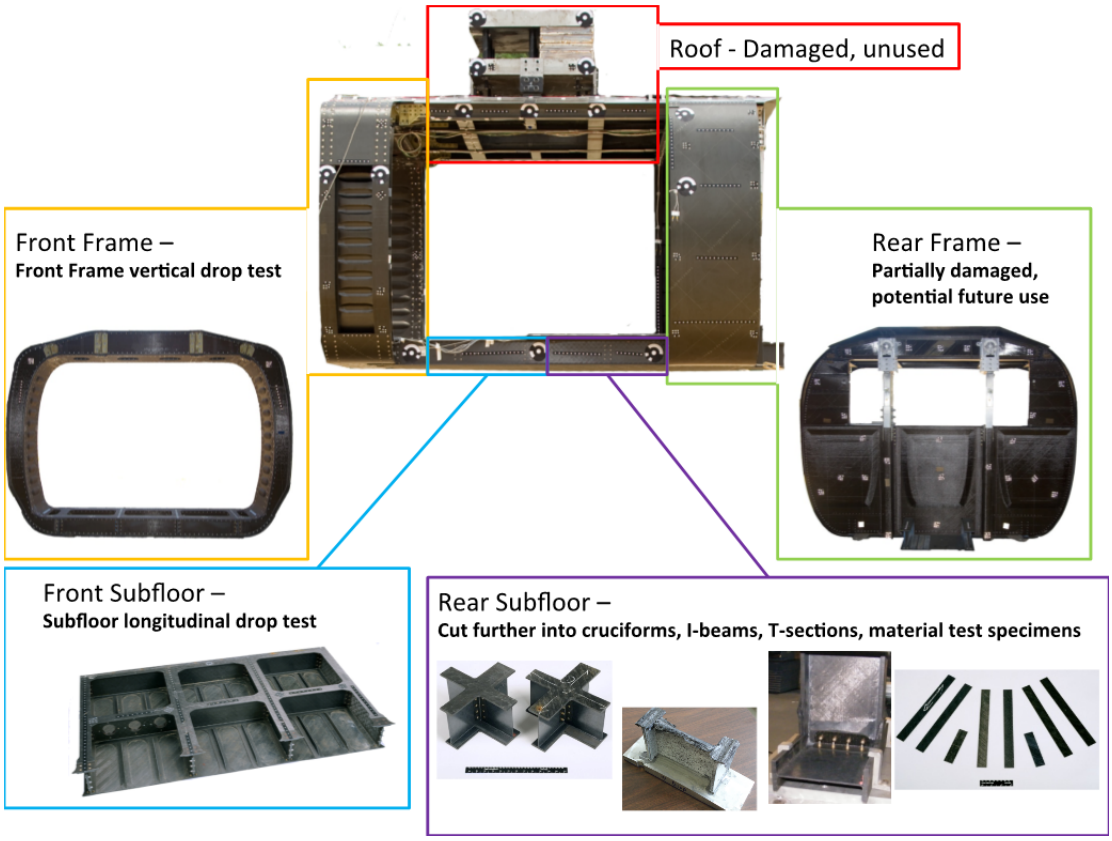

Figure 2. SARAP residual hardware utilization.

The SARAP TVA was manufactured of graphite unidirectional tape composite with a thermoplastic resin system that was cured using both autoclave and in situ techniques. However, the framed fuselage sections on either end of the TVA were constructed primarily of a plain weave graphite fabric material with a thermoset resin system. Since the TVA had been previously subjected to a fairly severe vertical impact test condition (252-in/s), it was necessary to evaluate the structural integrity of the test specimens extracted from the post-test TVA. Nondestructive Evaluation (NDE) methods were used to assess the smaller coupons and components. Results of these inspections showed that some areas of possible damage were identified for the larger components (I-beams, T-sections, and cruciform sections). However, no specific identifiable flaws were found [6]. Consequently, these specimens were tested.

Two I-beams, T-sections, and cruciform sections were extracted from the rear subfloor of the original SARAP TVA. These specimens were subjected to dynamic compressive loading. For each specimen type, one component was tested at a lower velocity while the second was tested at a higher velocity. For brevity, only one test condition will be described for each specimen type. For complete documentation, please see Reference 6. Also, it is important to note that the SARAP TVA was a prototype design, built by Sikorsky. To protect their data rights, specific details of the design including ply thicknesses, laminate stacking sequences, and material specifications are not provided.

Dynamic Crush Test of an I-beam Specimen

The I-beam specimen was 4.56-in. tall, 6.2-in. wide, with the lower end potted into a rigid foundation such that the main axis of the I-beam was oriented vertically. Corner notches with a chamfer angle of 45° were cut into the upper ends of the web to initiate specimen crushing and to reduce peak accelerations upon initial contact with the drop mass. A vertical test was conducted by releasing a 204.8-lb drop mass from a height of 4-ft using a 14-ft vertical drop tower, which impacted the upper end of the I-beam with a measured velocity of 189.6-in/s. Instrumentation included two accelerometers on the drop mass and a stochastic speckle pattern was painted on the I-beam web for collecting full-field strain photogrammetric data. A labeled schematic and photograph of an I-beam specimen are shown in Figure 3.

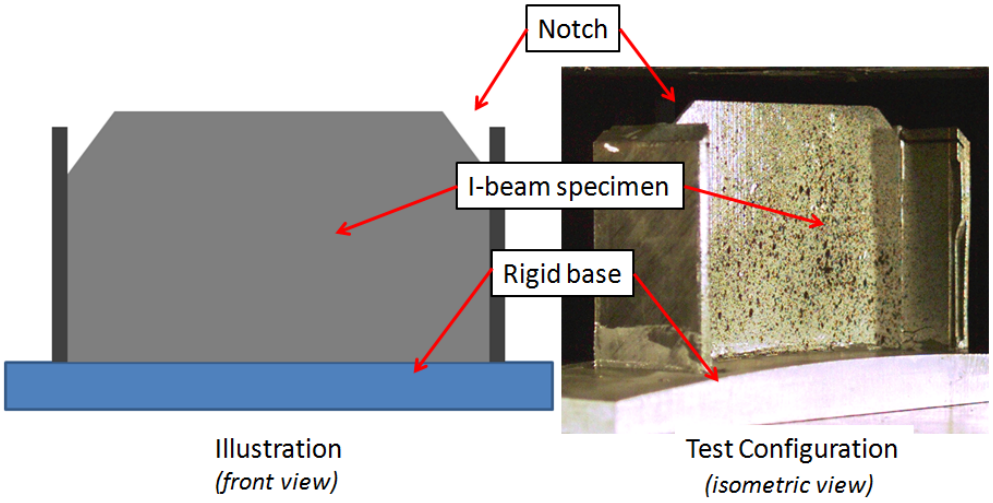

Figure 3. I-beam specimen configuration.

An image sequence of structural deformation is shown from the front face of the specimen in Figure 4. The upper left image in Figure 4 shows the specimen 1-ms before impact. The upper right image shows the specimen 1-ms after impact. At this time, the drop mass has begun crushing the upper edge of the web section, and has just contacted the outer flanges, which were approximately 1/16-in. shorter than the web. At 5-ms after impact, the top portion of the I-beam web is crushing with many of the composite layers delaminating and subsequently bending locally at the top of the web. The side flanges have begun to crush, but are not exhibiting significant amounts of delamination. At 10-ms after impact, material crushing and delamination from both the web and flanges can be seen. This time also corresponds to the approximate time of maximum displacement of the impact mass.

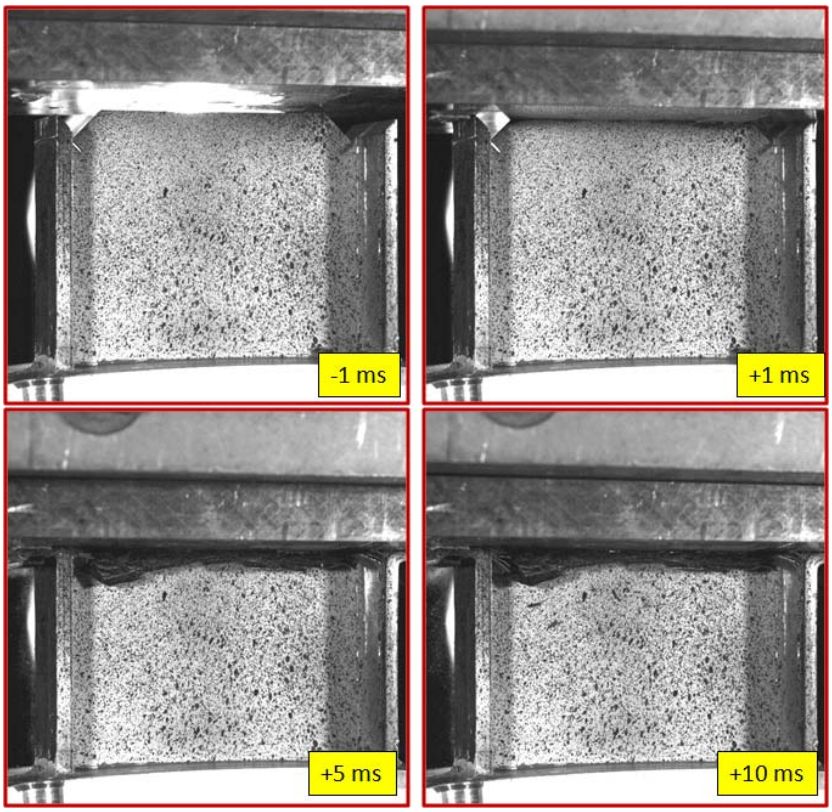

Figure 4. Image sequence of the I-beam 4-ft drop test.

Photogrammetric data were collected and sampled at 15 kHz. Compressive strains at two distinct times during the crushing sequence are shown in Figure 5. The compressive strain at 1-ms after impact, which occurs on the upward side of the acceleration curve is shown in Figure 5(a). The stress wave can be seen in the specimen by noting that, near the top where the drop mass is touching the specimen, strains are between -0.8 and -1.0 percent. The corners appear to have slightly larger strains, which could potentially be due to an uneven surface at the free edge of the specimen. However, the fixed end of the specimen exhibits between 0.0 and -0.2% strain, indicating that the stress wave has not travelled through the specimen and the strain is not fully developed at the fixed end.

The image shown in Figure 5(b) shows the compressive strain at 7.2-ms after impact, or, more specifically, the time of maximum acceleration. Layer delaminations and bending interfere with viewing of the uppermost edge of the crush front, so strains cannot be resolved up to the edge. However, by comparison of the two images, much of the middle region of the specimen that once exhibited -0.5% strain (in green) is now closer to 0.0% strain (in orange). The entire visible portion of the strain data on the specimen is exhibiting this low 0.0% value. These results indicate that the strain has become localized in the crush front. This finding is confirmed by examining the videos and pictures post-test. Visual inspections show that the majority of the specimen away from the crush front has stayed intact. Almost all of the damage has occurred at the crush front, and it is best characterized by layer delamination and bending with large amounts of material crushing.

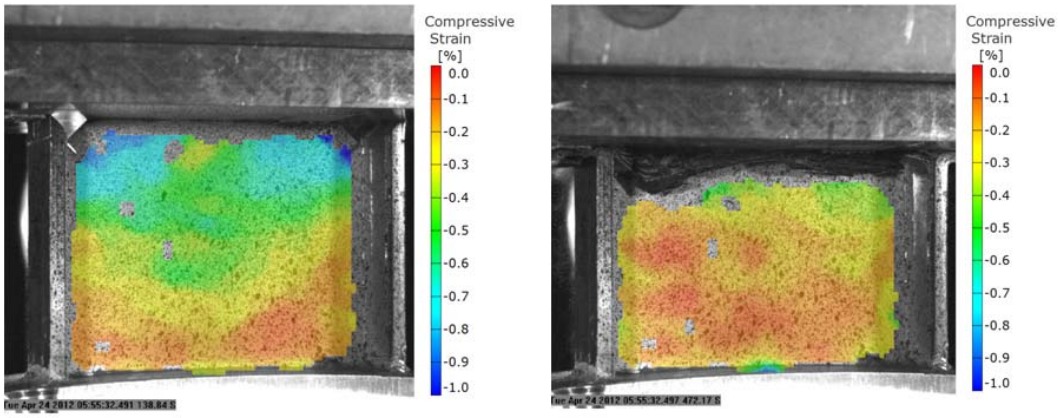

(a) Time = 1-ms. (b) Time=7.2-ms.

Figure 5. Compressive strain at 1-ms and 7.2-ms after impact of the I-beam.

A photograph of the specimen post-test is shown in Figure 6. The photogrammetric measurements are confirmed when looking at the failure patterns. The impact surface shows signs of ply delamination, material crushing, and localized bending, while the bottom of the specimen, which is fixed into the rigid base, exhibits no failure.

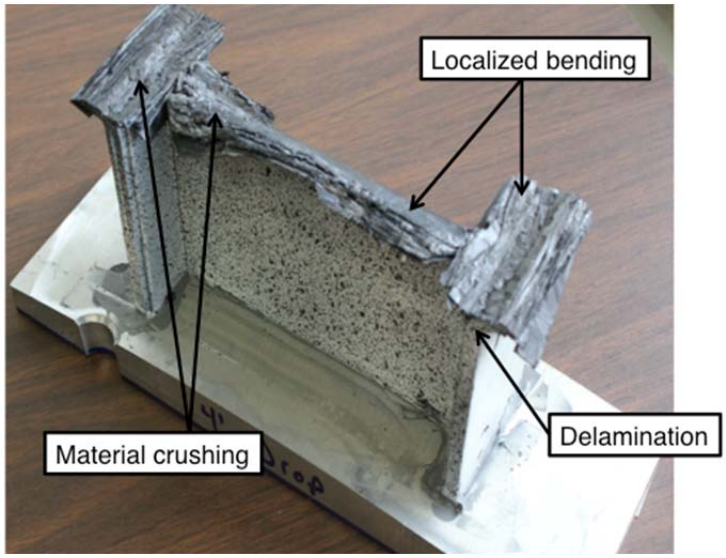

Figure 6. Post-test photograph of the I-beam tested at 4-ft drop height.

Dynamic Crush Testing of a T-Section Specimen

A T-section specimen was extracted from the edges of the subfloor where a lateral I-beam terminates at the edge of a longitudinal I-beam. At this termination point, the two I-beam sections on the floor were fastened together using doublers. When extracted, these specimens resembled a T shape. A drop test was conducted on the T-section using the 14-ft vertical drop tower, such that the lateral I-beam portion of the specimen is oriented in the vertical direction. This orientation ensures that initial contact with the large drop mass occurs at the end of the vertical flanges and web. The longitudinal subfloor I-beam was placed in a horizontal orientation, and used to support the vertical I-beam. The side flanges of the horizontal I-beam were clamped in four places to a large base fixture, which was fixed. A small aluminum bar (approximately 1-in. x 1-in. by 5.56-in.) was placed between the two inner flanges of the

horizontal I-beam and located in the center of the specimen, just beneath the vertical web. The bar was intended to react the compressive load applied to the vertical web to promote crushing rather than global buckling of the specimen. The specimen was impacted vertically to determine crush behavior, failure mechanisms, and energy absorbing characteristics of the I-beam layups and the composite doubler fasteners. Accelerometers were mounted to the drop mass and the vertical I-beam web was painted with a stochastic speckle pattern for use with photogrammetric techniques to collect full-field strain data. A picture of the T-section specimen in the test set-up is shown in Figure 7. The overall dimensions of the specimen were: 9-in. tall, 6.2-in. wide, and 13-in. long.

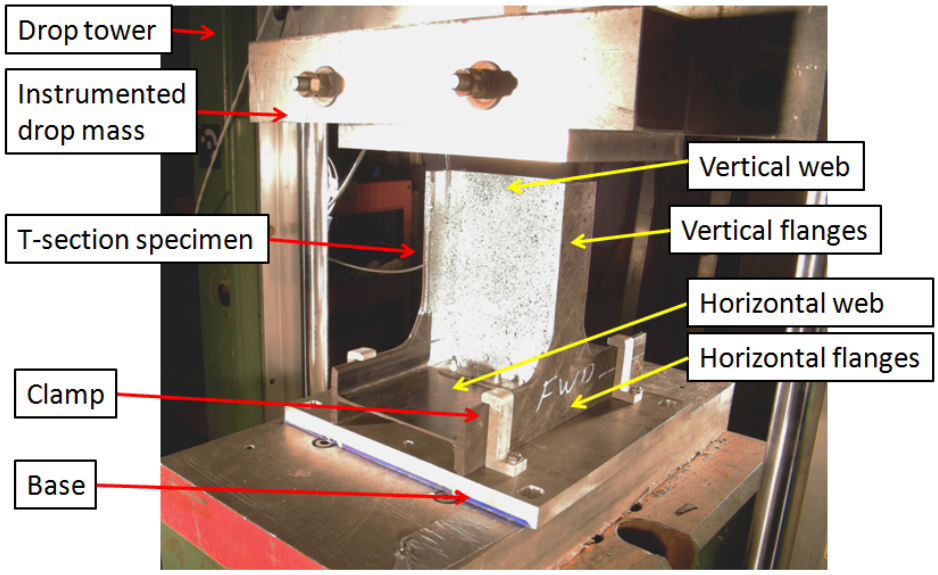

Figure 7. T-section test set-up.

The T-section drop test was conducted by releasing the 204.8-lb drop mass from a height of 4-ft, producing a measured impact velocity of 192-in/s. An impact sequence is shown in Figure 8. The upper left image in Figure 8 shows the specimen 1-ms before impact. The upper right image shows the specimen 1-ms after impact. By this time, the vertical flanges have failed completely above the fillet. At 5-ms after the impact, the vertical I-beam has separated from the horizontal I-beam and the energy of the drop mass is crushing the web of the vertical I-beam into the doubler region. At 20-ms after impact, the impact mass has reached maximum crush displacement. The lower right image shows failure of the vertical I-beam's web, flange and doubler region.

Cameras were used to film the front web of the T-section, sampling at 10 kHz. Two fringe plots are shown at 0.5-ms after initial impact in Figure 9. The photogrammetric data show large amounts of out-of-plane motion in the vertical web of the specimen. The out-of-plane behavior resembles an "oil canning" mode of motion with opposite out-of-plane motion on the top and bottom separated by a zero datum in the middle. A contour plot of compressive strain on the surface of the specimen is shown in Figure 9(b). The majority of the web is exhibiting low (between 0 and -0.25%) compressive strain. However, the web/doubler junction exhibits large variations in strain, as indicated by the blue-green region near the bottom of Figure 9(b). The web exhibits considerable out-of-plane motion; however, primary failures occur near the base of the web at the doubler region and at the vertical flanges located just above the fillets.

Delaminations of the vertical flanges created a complete line of fracture, separating the flange into two parts. This separation allowed the upper flange to become wedged inside the lower structure.

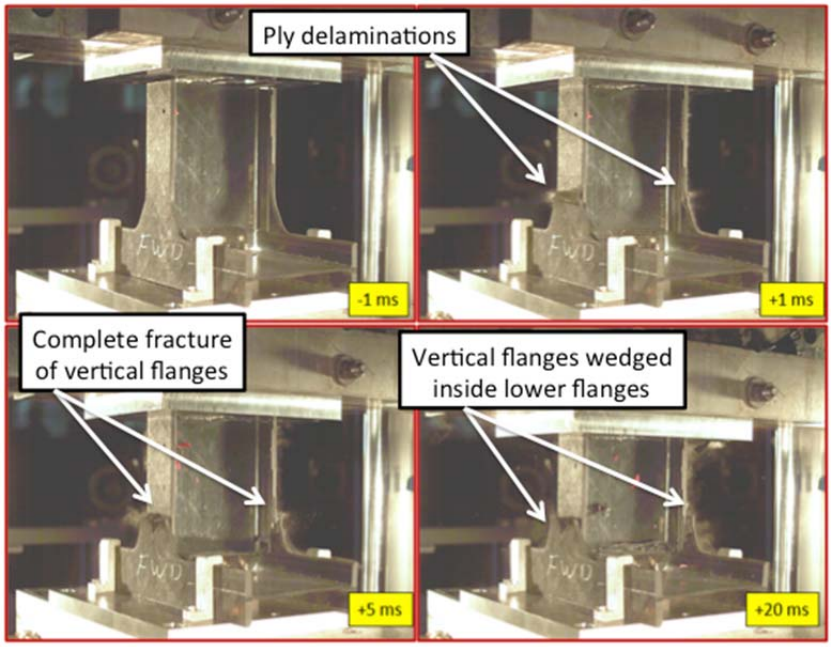

Figure 8. Image sequence of the 4-ft T-section test.

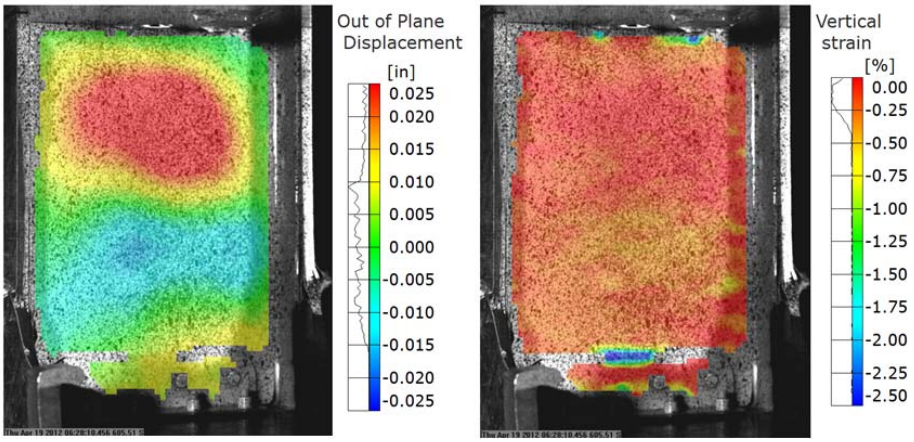

(a) Out-of-plane displacement. (b) Compressive strain.

Figure 9. Photogrammetry results for 4-ft T-section drop test, 0.5-ms after impact.

The photogrammetric data are confirmed by examining the post-test photographs shown in Figure 10. Both the front and back views show complete failure of the doubler region between the vertical and horizontal I-beam webs. Furthermore, these photographs show a complete shear failure of the composite layers on the vertical flanges, near the transition region between vertical and horizontal. This evidence supports the conclusion that the specimen failed near the boundary edges. Thus, the T-section test proved to be less of a demonstration of a pure material failure, and more of an examination of the influence of test and boundary conditions.

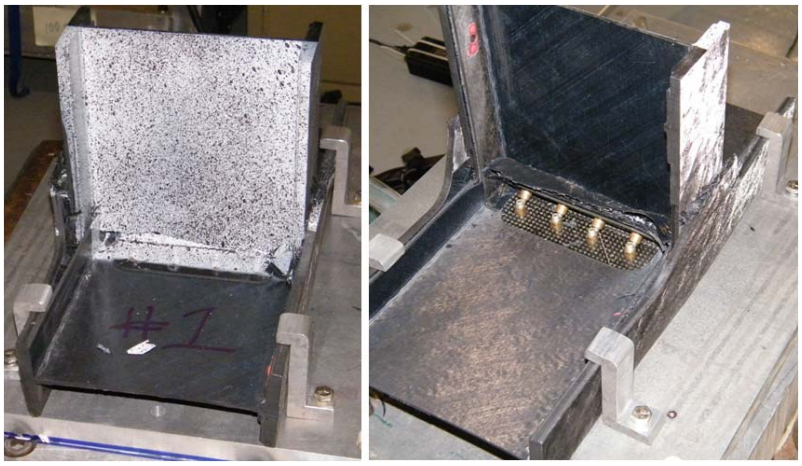

(a) Front view. (b) Rear view.

Figure 10. Post-test photographs of the T-section following the 4-ft test.

Dynamic Crush Testing of a Cruciform Section

A cross-shaped cruciform section located at the junction of a longitudinal and lateral I-beam was extracted from the subfloor of the post-test TVA. The length of each quadrant was approximately 6 in., which made the entire specimen a 12-in. by 12-in. cross. Each cruciform was approximately 6 in. tall. A photograph of a cruciform test specimen is shown in Figure 11.

Figure 11. Photograph of a cruciform section test specimen.

The cruciform specimen was impacted using a 14-ft vertical drop tower to determine its crush behavior, failure patterns and mechanisms, and energy absorbing characteristics. During the test, the top flange was impacted by the drop mass, while the bottom flange remained fixed. Two quadrant faces were painted with a stochastic speckle pattern for use with full-field strain photogrammetric techniques. Accelerometers were mounted on the drop mass to measure impact acceleration and crush displacement. The 215-lb drop mass was released from a height of 8-ft, which impacted the cruciform at a measured impact velocity of 268.6-in/s.

An image sequence of the impact is shown in Figure 12. The image in the upper left shows the specimen immediately before impact. This view shows one cruciform quadrant on the left side, one on the right side and one in the middle perpendicular to the camera view. The upper right

image shows the specimen 1-ms after impact. At this time, failure has already occurred through crushing on the left side quadrant, and delamination in the perpendicular face. The lower left image shows the cruciform 2-ms after impact. Failures are present in all three visible quadrants. Finally, the lower right image in Figure 12 shows the cruciform 15-ms after impact at which point the drop mass has reached maximum crush displacement.

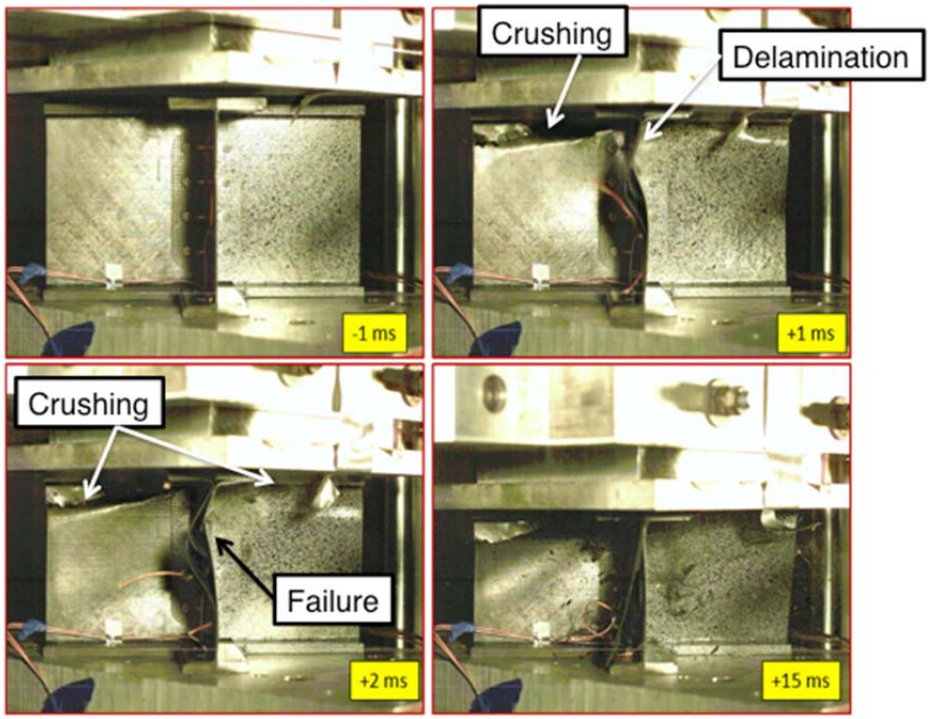

Figure 12. Image sequence of cruciform crush during the 8-ft drop test.

Photogrammetric measurements were of limited success because of lower film rates due to equipment availability. Finally, the specimen is shown in post-test photographs in Figure 13. Massive failure is evident throughout the specimen. Large areas of debonding and ply delamination are observed in all four quadrants. A noticeable crush front is observed near the top of the specimen. Also, part of the doubler region, which is the strongest part of the entire specimen, has failed. Due to the large amount of damage in the specimen, it was possible to remove entirely the top flange away from the rest of the specimen due to the failures near the crush front.

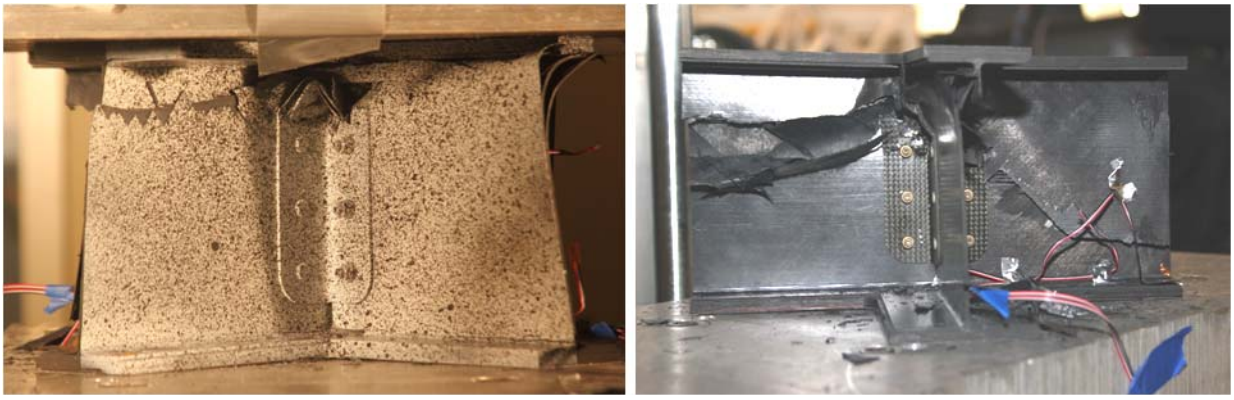

Figure 13. Post-test images of cruciform specimen following the 8-ft drop test.

Model Development and Test-Analysis Comparisons

Finite element models were developed to represent each of the component test articles and simulations were conducted using LS-DYNA. Within LS-DYNA, two composite material models were evaluated: MAT_ENHANCED_COMPOSITE_DAMAGE (Mat 54), a progressive failure model that uses the Chang-Chang failure criterion to simulate ply-by-ply failure and property degradation and MAT_LAMINATED_COMPOSITE_FABRIC (Mat 58), a continuum damage mechanics model for representing unidirectional tape and fabric composite materials. A brief description of these two material models is provided. In addition, this section of the report will describe the finite element models of each component and provide test-analysis comparisons of time-history responses and experimental and predicted structural deformations. Note that for displacement-time histories, data from double-integration of the accelerometers, as well as data obtained from photogrammetric measurements, are plotted with predicted responses.

Material Modeling

The LS-DYNA material property designated MAT_ENHANCED_COMPOSITE_DAMAGE or (Mat 54) [5], was selected for evaluation in this study. Mat 54 material properties were provided by Sikorsky. This material model is used to represent orthotropic materials, such as composite laminates fabricated of unidirectional tape material, and should be limited to thin shell construction. Composite lamination theory is used to determine ply stresses and strains in the laminate. Two different failure criteria can be specified including Chang-Chang [8, 9] or Tsai-Wu [10], by setting the CRIT parameter to 54 for Chang-Chang, or 55 for Tsai-Wu in the Mat 54 card. For all of the Mat 54 simulations presented in this document, CRIT was set to 54. The Chang-Chang failure criterion is a progressive in-plane damage model that accounts for three in-plane failure modes: matrix cracking, fiber-matrix shearing, and fiber breakage. The nonlinear shear stress-strain behavior is based on the theory described in References 11 and 12. For fiber failure and/or fiber-matrix shearing, the level of property degradation within the damaged area depends on the size of damage predicted by the fiber failure criterion [13]. Note that most progressive failure models are strength-based. When the strength of a ply within the laminate is exceeded, the properties are degraded. Progressive failure is achieved through ply-by-ply failure within the laminate. Once all plies in the laminate have failed, the element is deleted.

Mat 54 incorporates a set of model-specific parameters that influence material failure behavior, but that cannot be measured in a laboratory. Some of these parameters include TFAIL, SOFT, ALPH, YCFAC, FBRT, BETA, and EFS. If utilized, these parameters must be determined through analytical calibration studies, or by trial and error. Reference 14 provides an excellent description of these parameters, along with the results of parametric studies showing how changes in these parameters can influence model responses.

Mat 58 is a continuum damage mechanics material model based on the Matzenmiller-Lubliner-Taylor theory [15] and is intended for use with shell elements to simulate composite tape laminates and woven fabrics. The model requires input of material properties in tension, compression, and shear to define stress-strain behavior within the lamina or laminate. The user specifies the in-plane elastic modulus and Poisson's ratio in two primary directions, designated A and B in LS-DYNA. Maximum strength values in tension, compression, and shear are also specified at corresponding strain values. The tensile response is initially linear elastic with the modulus specified by EA. Stress increases nonlinearly until XT, the maximum strength, is reached. The nonlinear portion of the response is defined internally by LS-DYNA based on a

continuum damage mechanics theory [15]. Once XT is reached, the stress is reduced based on the "stress limiting" factor SLIMT1, and is then held constant at the reduced value until elements reach a strain specified by the ERODS parameter in the material model, at which point the elements are deleted and removed from the solution. Through the appropriate selection of the SLIM parameters and ERODS, it is possible to incorporate plastic-like behavior in the model and avoid pre-mature element failure. Similar stress-strain responses are defined for in-plane compression and shear. Reference 16 provides an excellent description of continuum damage mechanics based composite failure models and gives an excellent assessment of Mat 58 for predicting energy absorption of composite materials. Additional information on this material model can also be found in Reference 5.

Simulation of a Dynamic Crush Test of an I-Beam Specimen

A finite element model, depicted in Figure 14, was developed to simulate dynamic crushing of the I-beam specimens. The model consisted of 24,300 nodes; 3,050 Belytschko-Tsay (ELFORM=Type 2) quadrilateral shell elements representing the I-beam with a nominal element edge length of 0.125-in.; and 16,400 solid elements representing the drop mass. Either Mat 54 or Mat 58 were assigned to the shell elements representing the I-beam, whereas Mat 20 (MAT_RIGID) was assigned to the drop mass. The density of the rigid material was adjusted to ensure that the weight of the drop mass matched that of the test (204.8-lb). Seven different parts were used including one part for the drop mass, and six parts representing different regions of the I-beam. Several different PART_COMPOSITE cards were created to represent the upper edges of the I-beam flanges that incorporated ply drop-offs to mimic the reduced thicknesses produced by chamfering. I-beam models were executed using LS-DYNA SMP Version 971 R6.0.0 with double precision and required 5 hours and 51 minutes of CPU on four Linux-based processors for an end time of 0.02-s. Two SPC definitions were used, one to fix the bottom nodes of the I-beam, and the second to ensure that the drop mass could move only in the vertical direction. Finally, the nodes forming the drop mass were assigned an initial velocity to match the test condition of 189.6-in/s. Output from the model included acceleration-, velocity-, and displacement-time histories of a central node on the drop mass, as well as pictures of model deformation.

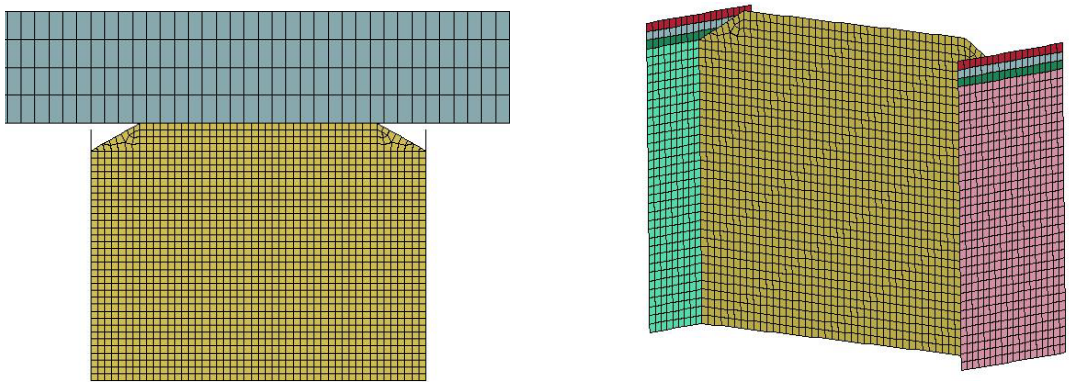

(a) Front view with drop mass. (b) Three-quarter view without drop mass.

Figure 14. LS-DYNA model of the I-beam component.

Poor results were obtained using the Mat 54 material model. Essentially, the model failed in a brittle fashion, exhibiting very little energy absorption. Numerous parameter studies were conducted in an attempt to obtain stable crushing of the model. However, all models provided

similar results to those shown in Figure 15. Predicted acceleration responses consisted of a series of spikes representing repeated contact and release of the drop mass onto the I-beam. These short-duration spikes occur early in the pulse. Only 50-in/s of velocity is removed during the simulation through failure of the I-beam. As indicated in Figure 15(c), the vertical displacement of the drop mass is not alleviated and it continues to displace linearly without abatement. The model fails catastrophically with no sign of stable crushing, as shown in Figure 16. The model loses the bottom nodal constraints, as elements are failed and removed.

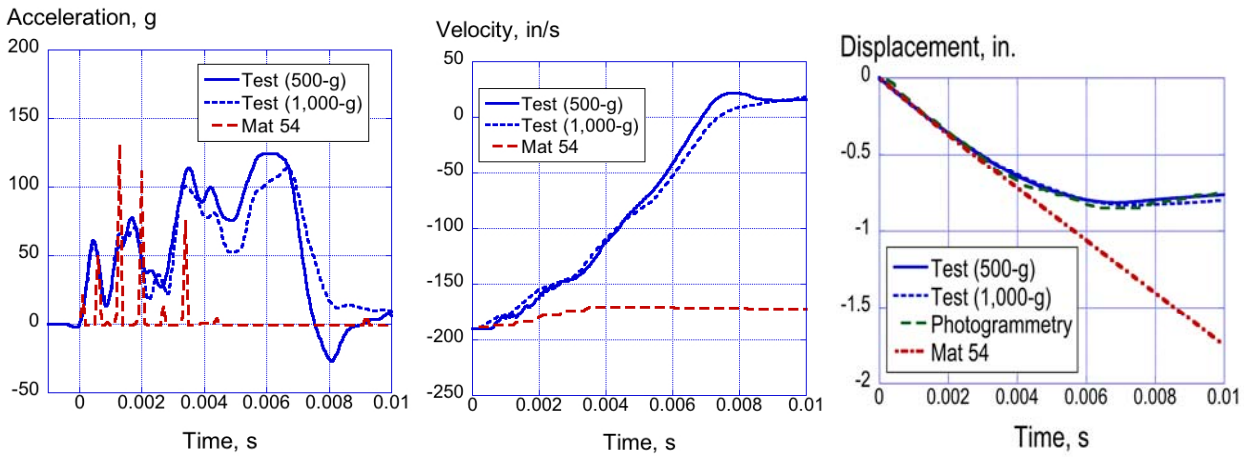

(a) Acceleration. (b) Velocity. (c) Displacement.

Figure 15. Experimental and Mat 54 analytical results for the I-beam crush test at 189.6-in/s.

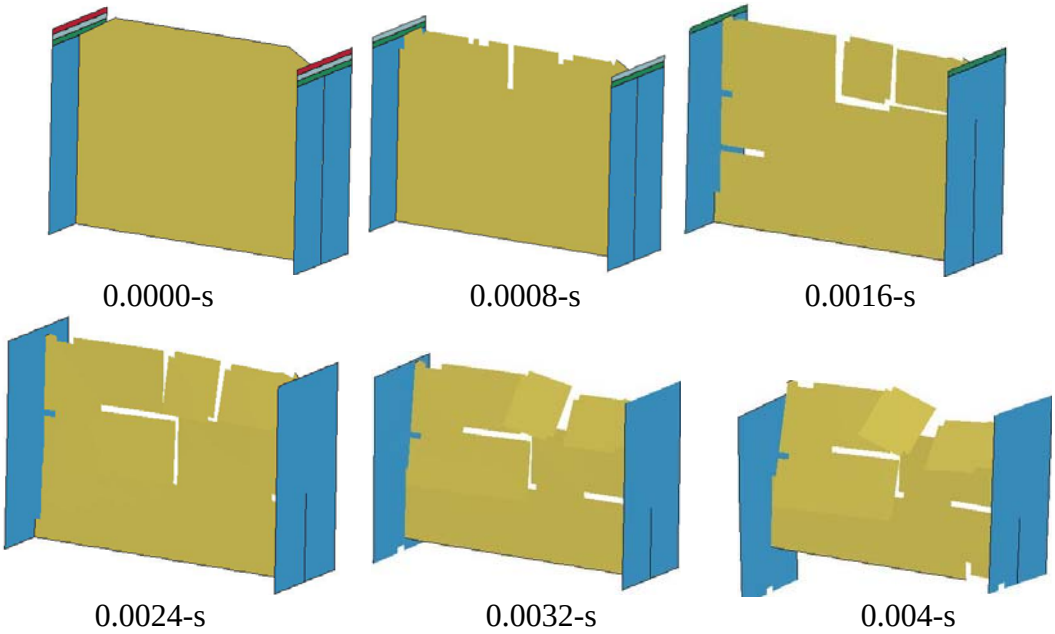

Figure 16. Mat 54 model predicted deformation pattern indicating complete specimen collapse.

The Mat 58 predicted responses show good agreement with the overall shapes, magnitudes, and pulse durations of the experimental curves, as shown in Figure 17. The experimental and predicted acceleration responses were filtered using a 1000-Hz Butterworth low-pass filter. The displacement results, shown in Figure 17(c), include the Mat 58 predicted response, the

responses based on double integration of the acceleration data and photogrammetry. The maximum crush displacement predicted by the model (0.85-in.) falls between the experimental results (0.82- to 0.86-in.). A sequence of model deformation is shown in Figure 18 for four time steps. These depictions show that the I-beam model exhibits stable crushing from the top edge, matching the deformation patterns of the test article, depicted in Figure 4. No global buckling is evident, though some folding of the webs is observed.

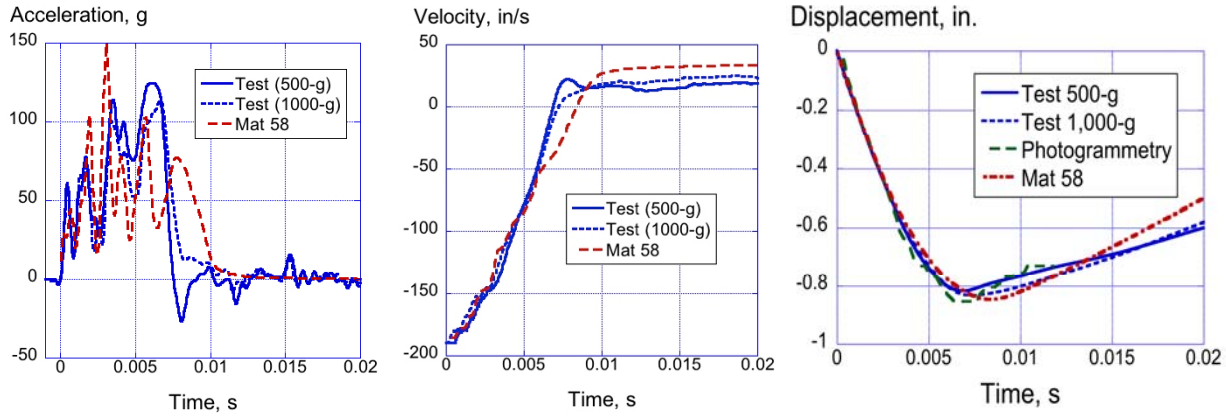

(a) Acceleration. (b) Velocity. (c) Displacement.

Figure 17. Experimental and Mat 58 analytical results for the I-beam 4-ft. drop test.

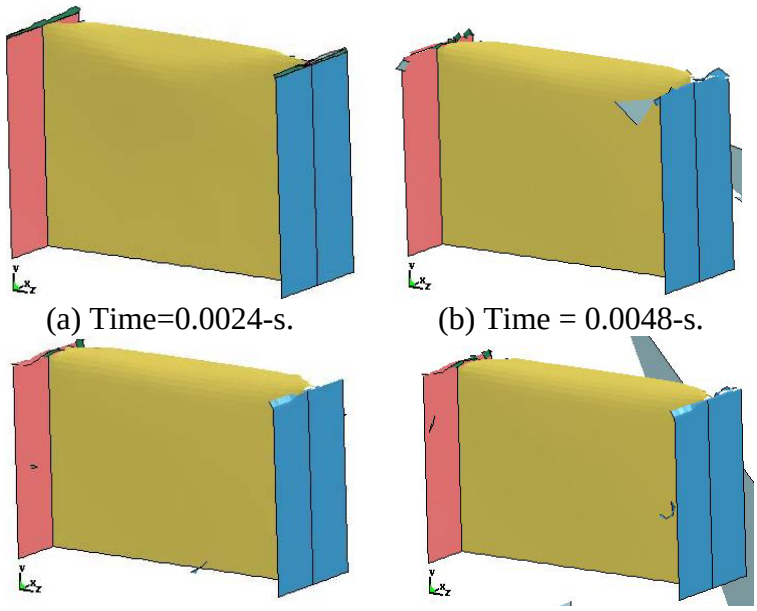

(a) Time=0.0024-s. (b) Time = 0.0048-s.

(c) Time=0.0072-s. (d) Time = 0.01-s.

Figure 18. Time sequence of I-beam model deformation for Mat 58.

A parameter study was conducted to evaluate the influence of ERODS, which is a Mat 58 input term that controls element deletion. For this evaluation, ERODS was varied from 0.1 to 0.5 in increments of 0.1. Displacement-time history results are shown in Figure 19. The ERODS study indicates that a value of 0.5 provides best agreement with test data.

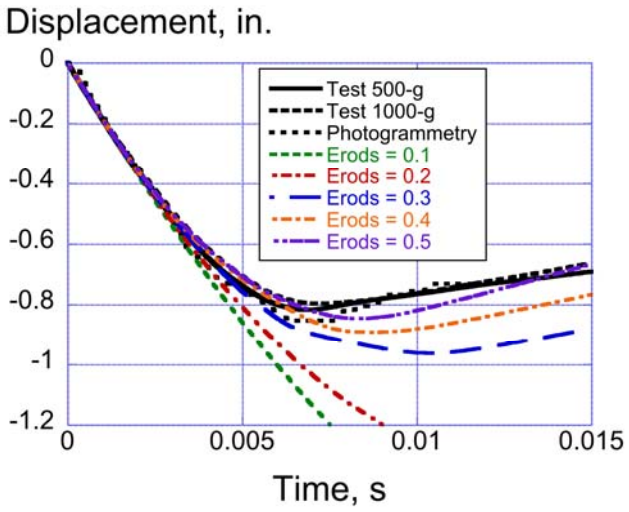

Figure 19. Mat 58 ERODS parameter study results for the I-beam (189.6-in/s velocity).

Simulation of a Dynamic Crush Test of a T-Section Specimen

A finite element model, shown in Figure 20, was developed to represent the 4-ft (192-in/s) dynamic impact test of a T-section component. This T-section model incorporated four fillets, which are located at the intersection of the vertical and horizontal flanges. The model consists of: 15,367 nodes; 13,746 quadrilateral shell elements; 512 solid elements to represent the drop mass; 9 parts; 3 material models; 2 constraint definitions; and, one contact definition. For all simulations, Belytscko-Tsay shell elements were used (ELFORM=Type 2). Mat 54 or Mat 58 were assigned to the shell elements representing the T-section, whereas Mat 20 (MAT_RIGID) was assigned to the drop mass. The density of the rigid material was adjusted to ensure that the weight of the drop mass matched that of the test.

Two SPC definitions were used, one to fix the bottom nodes of the horizontal I-beam flanges, and the second to ensure that the drop mass could move only in the vertical direction. Finally, the nodes forming the drop mass were assigned an initial velocity to match the test condition of 192-in/s, corresponding to the 4-ft drop height. Output from the model included acceleration-, velocity-, and displacement-time histories of a central node on the drop mass, as well as pictures of model deformation. The nominal element edge length was 0.125-in. Simulations were executed for 0.04-s, which required 8 hours of CPU on four Linux-based processors.

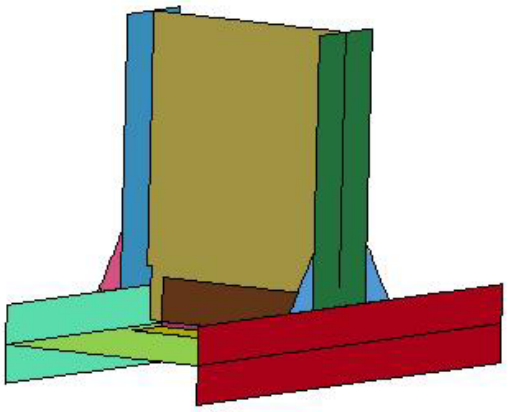

Figure 20. T-section finite element model (drop mass not shown).

The T-section model with Mat 54 properties rapidly disintegrates as shown in Figure 21, which depicts a series of model deformation at five time increments. Multiple element failures are observed in different regions of the model, most of which do not match the test response. The acceleration- and displacement-time histories of the drop mass are compared with test data in Figure 22. The test-analysis comparisons are poor.

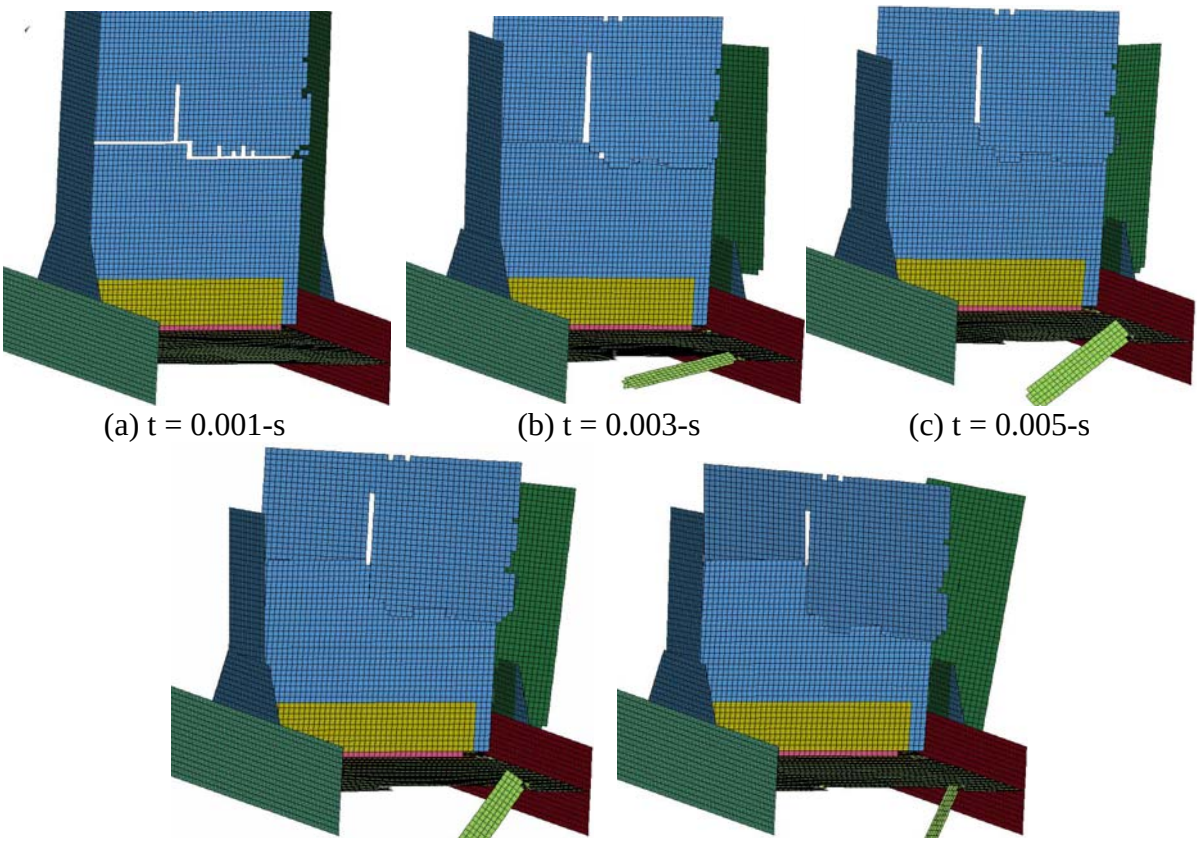

(a) t = 0.001-s (b) t = 0.003-s (c) t = 0.005-s

(d) t=0.007-s (e) t = 0.009-s

Figure 21. Mat 54 T-section model deformation.

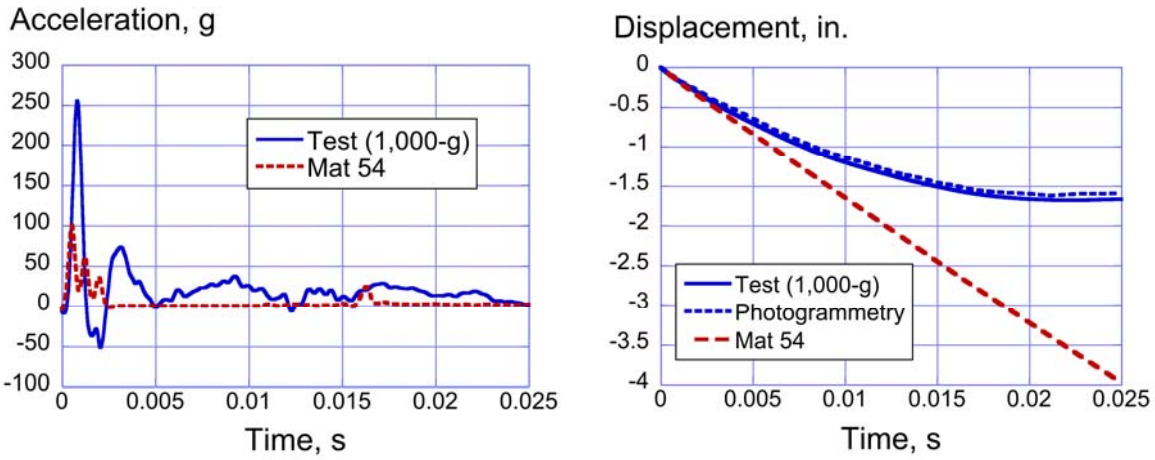

(a) Acceleration comparisons. (b) Displacement comparisons.

Figure 22. Comparisons of the 4-ft drop test data with the Mat 54 model predictions.

For Mat 58, the initiation of failure occurred as buckling of the vertical I-beam flanges above the fillet. In the test, delaminations caused complete failure of the flange, allowing the flanges on both sides above the fillets to become wedged inside the horizontal flanges below the fillets. Comparisons of the test and Mat 58 predicted acceleration, velocity, and displacement responses are shown in Figures 23(a), (b), and (c), respectively. Both test and analytical acceleration responses have been filtered using a 1000-Hz low-pass Butterworth filter. The Mat 58 model shows three peak accelerations whereas the test only shows two. However, the peak accelerations are comparable in magnitude to the test.

The displacement is much lower for the model than the test as is evident in Figure 23(c). The displacement disparity can be explained by observing the failure mechanism in the test and comparing with the simulation. Although the vertical flanges in both the test and model completely failed above the fillet, in the test the vertical flanges wedged inside the horizontal flanges below the fillet. However, in the model (see Figure 24), the vertical flange rotated slightly after failing, which allowed edge-on-edge contact with the horizontal flange after failure. Since single surface contact was used, this contact allowed the upper flange to react against the lower flange. The higher force generated prevented further displacement from occurring after 0.01 seconds, whereas the actual test specimen continued displacing up to 0.02 seconds. The final deformation pattern of the model is illustrated in Figure 24.

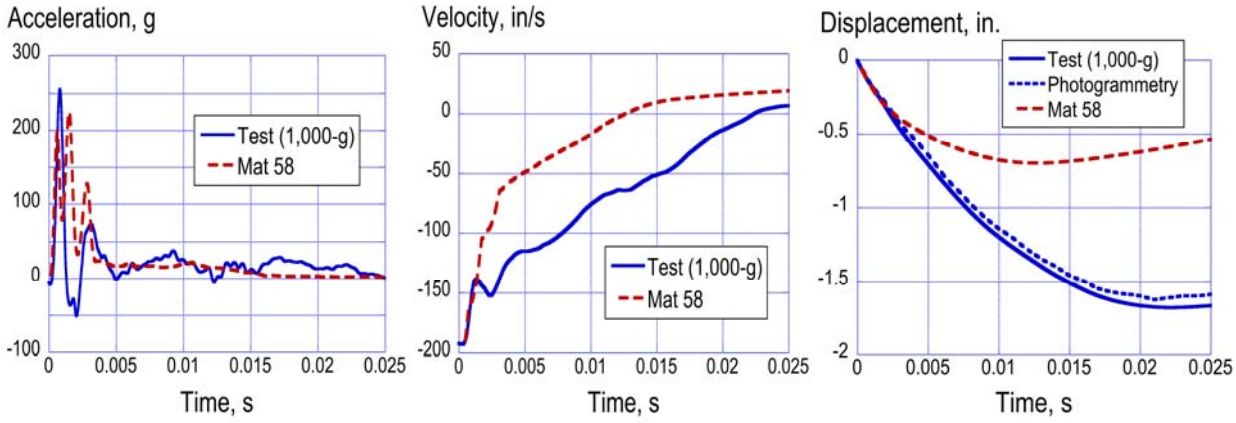

(a) Acceleration. (b) Velocity. (c) Displacement.

Figure 23. Comparisons of Mat 58 model predicted responses with 4-ft T-section test data.

As with the I-beam model, an ERODS parameter study was conducted in which ERODS was varied from 0.1 to 0.5 in increments of 0.1. The deformation and failure of the model varied considerably with the ERODS value. Consequently, there is no uniformity of results and there is no convergence, as shown in Figure 25. Although the displacement response for an ERODS value of 0.1 most closely matches the test data, the actual deformed model, shown in Figure 26(a), failed catastrophically and does not compare favorably with the post-test damage. The best deformation results are obtained with an ERODS of 0.2. The deformed shape shown in Figure 26(b) is similar to the observed damage with both vertical flanges failing above the fillets. However, the damage near the top of the vertical web did not occur in the test.

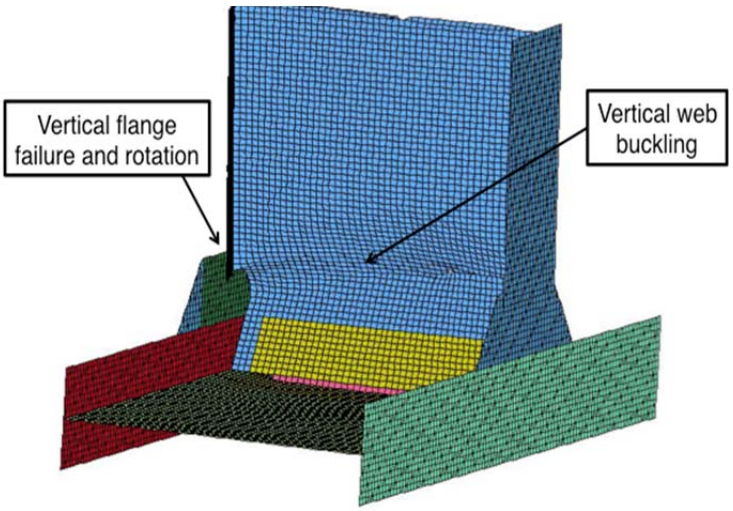

Figure 24. Mat 58 predicted damage of the T-section model at time 0.015 seconds after impact.

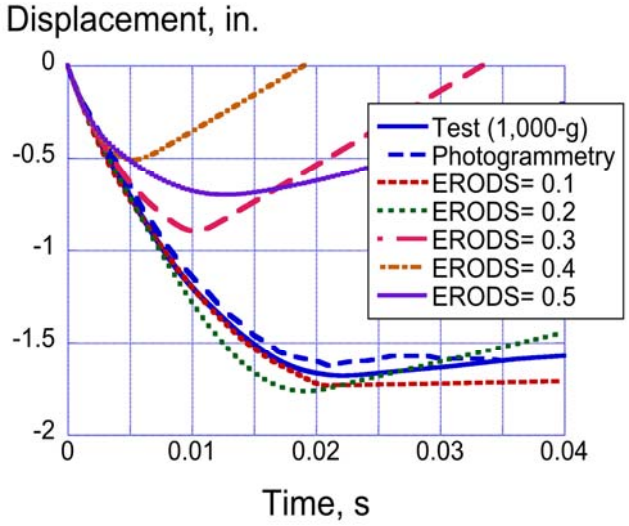

Figure 25. Test-analysis displacement responses with varying ERODS parameter.

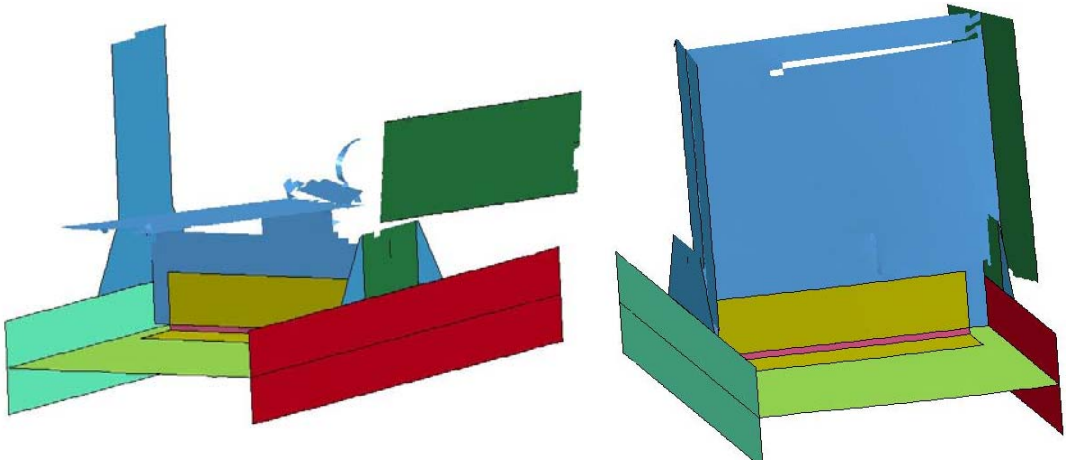

(a) Deformed model for ERODS = 0.1 (b) Deformed model for ERODS = 0.2

Figure 26. Mat 58 T-section model deformation for ERODS = 0.1 and 0.2.

Simulation of the Dynamic Crush Test of a Cruciform Section

Two views of the cruciform section finite element model are depicted in Figure 27. The model consists of 16,916 nodes; 15,750 Belytschko-Tsay quadrilateral shell elements representing the cruciform; and, 512 solid elements representing the drop mass. Ten parts were defined, one part for the drop mass and nine parts for the cruciform, including four flange parts, two web parts, and three separate parts defining the center clips. Five material cards were defined including Mat 20 (MAT_RIGID) for the impact mass. Four different Mat 54 or Mat 58 cards were required to ensure consistent and correct local material axis directions. These were input by setting AOPT = 2.0, which specifies that the local material axis directions are defined using vector input [5]. The density of the rigid material was selected to match the weight (215-lb) of the experimental drop mass.

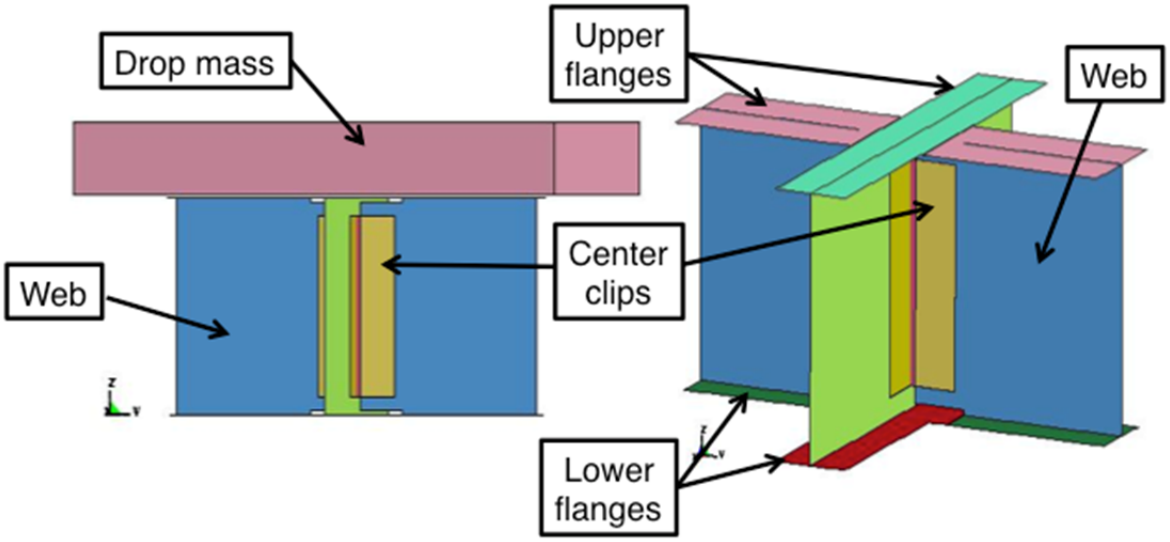

Figure 27. Depictions of the cruciform model.

Two SPCs were defined, one to allow the drop mass to move in the vertical direction only and one to fix the nodes of the bottom flanges. Finally, the nodes forming the drop mass were assigned an initial velocity to match the test condition of 268.6-in/s, which corresponds to the 8-ft drop height used during the test. Output from the model included acceleration-, velocity-, and displacement-time histories of a central node on the drop mass, as well as pictures of model deformation. The cruciform model was executed using LS-DYNA SMP Version 971 R6.0.0 with double precision and required 13 hours and 21 minutes of CPU on four Linux-based processors for an end time of 0.03-s.

Results are shown in Figure 28 comparing the 268.6-in/s drop test data with the Mat 54 predicted responses. The acceleration responses shown in Figure 28(a) have been filtered using a Butterworth 1000-Hz low pass filter. The experimental acceleration response exhibits a high spike initially, followed by a somewhat stable crushing phase. However, the model is not able to capture any feature of the test response. The velocity comparison, shown in Figure 28(b), indicates that kinetic energy is removed from the test and the drop mass crosses zero velocity at 0.015-s. Conversely, the model shows that only 120-in/s of velocity was removed from the simulation during the same time period. The displacement plot, shown in Figure 28(c) indicates that while the test curve exhibits a maximum crush stroke of 1.63-in., the predicted response continues to displacement vertically without abatement.

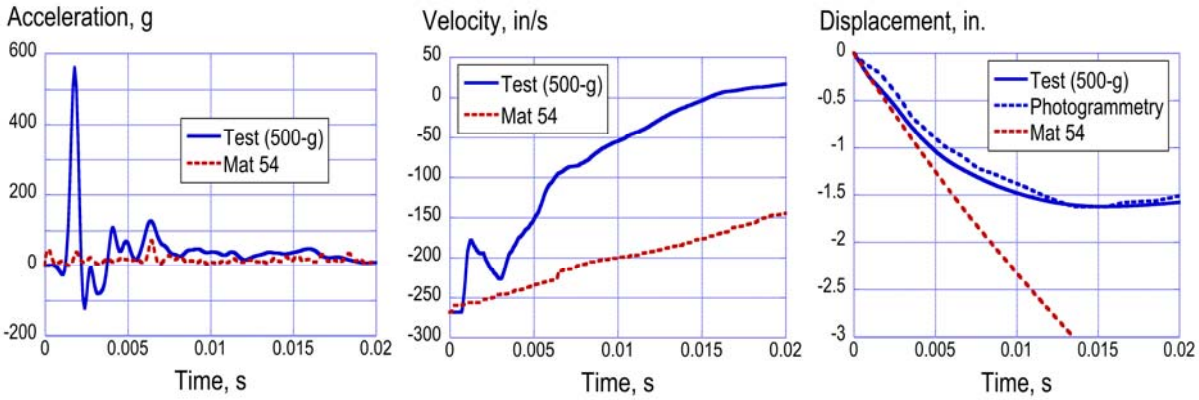

(a) Acceleration. (b) Velocity. (c) Displacement.

Figure 28. Experimental and Mat 54 analytical results for the cruciform 8-ft. drop test.

Four depictions of the Mat 54 model deformation are shown in Figure 29 for the simulation of the 268.6-in/s vertical drop test of a cruciform specimen. The model fails in a brittle fashion, with no evidence of bending or buckling. By 0.01-s, the interface elements between the web and flanges have failed and been removed from the simulation. These element failures allow the webs to separate from the flanges, and as the simulation continues, part-to-part contact forces the broken webs to rotate sideways. The predicted deformation pattern does not match the observed experimental results, which are depicted in Figure 12.

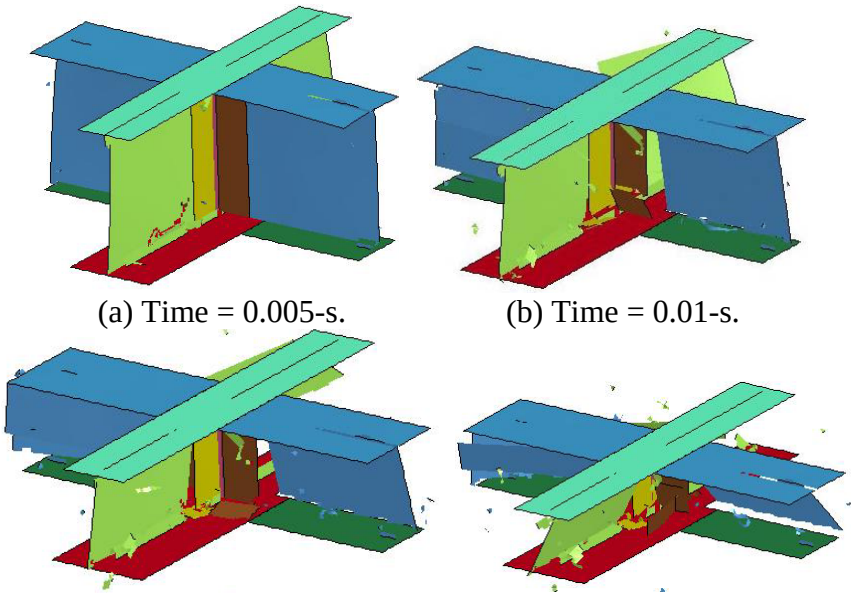

(a) Time = 0.005-s. (b) Time = 0.01-s.

(c) Time = 0.015-s. (d) Time = 0.02-s.

Figure 29. Mat 54 cruciform model deformation (velocity = 268.6-in/s).

The cruciform model was re-executed with Mat 58 material properties for an impact velocity of 268.6-in/s, representing the 8-ft drop test condition. Experimental and analytical acceleration-, velocity-, and displacement-time histories are compared in Figure 30. Note that the acceleration curves shown in Figure 30(a) were filtered using a Butterworth 1000-Hz low pass filter. The test acceleration exhibits an oscillatory response with a high initial peak acceleration of

approximately 550-g. The predicted response also exhibits an initial peak acceleration (163-g), which is much lower in magnitude than the test response. Following the initial spike, the two curves are close in magnitude and duration. Further verification of the level of agreement is seen in the velocity and displacement responses, shown in Figures 30(b) and (c), respectively. The predicted velocity curve exhibits a significant change in slope early in the response and essentially averages the oscillations in the test response. The maximum predicted crush displacement is 1.68-in., which compares well with the test value of 1.63-in. Also, note that the photogrammetric results indicated a consistent maximum crush displacement of 1.63-in.

Model deformations are shown in Figure 31 for six time steps. These depictions indicate severe buckling and bending of the webs; however, few if any elements are removed from the model. Also, the integrity of the web-flange interface is maintained. The predicted deformation pattern is a reasonably good match to the test response, which is shown in Figure 12.

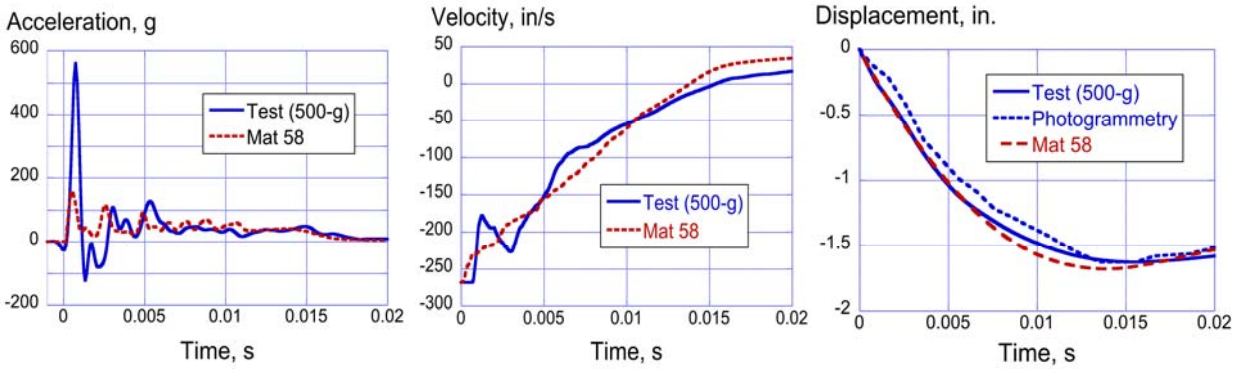

(a) Acceleration responses. (b) Velocity responses. (c) Displacement responses.

Figure 30. Experimental and Mat 58 analytical results for the cruciform 8-ft. drop test.

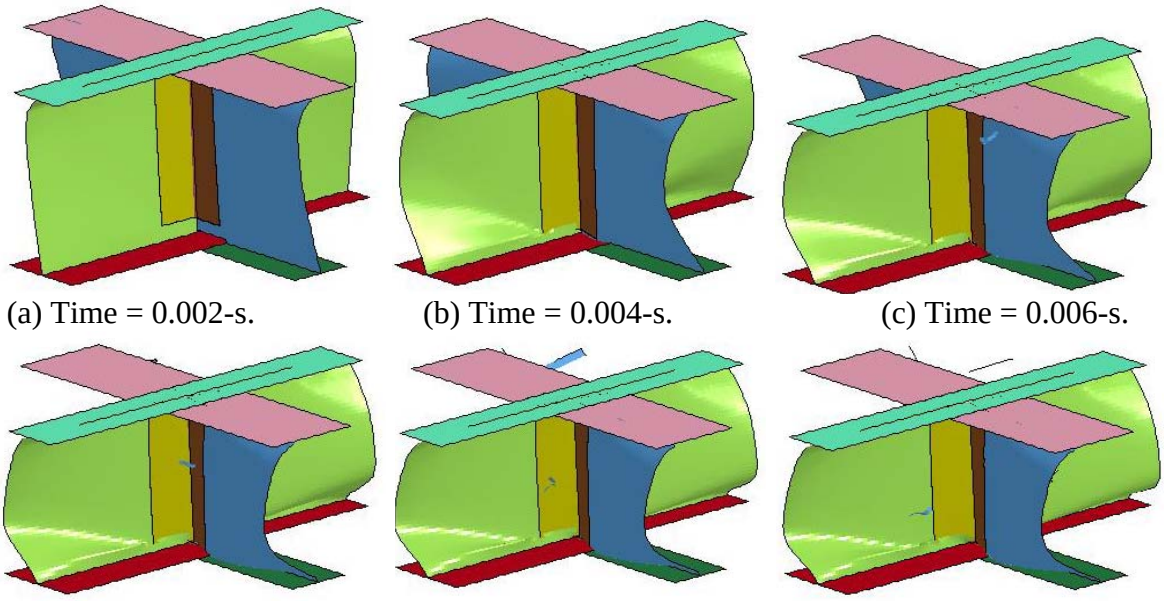

(a) Time = 0.002-s. (b) Time = 0.004-s. (c) Time = 0.006-s.

(d) Time = 0.008-s. (e) Time = 0.01-s. (f) Time = 0.012-s.

Figure 31. Mat 58 cruciform model deformation sequence (velocity = 268.6-in/s).

An ERODS study was conducted for the Mat 58 model of the cruciform section in which ERODS was varied from 0.1 to 0.5 in increments of 0.1. The results for this parameter study are shown in Figure 32. The ERODS study indicates that a value of 0.5 provides the best agreement with test data.

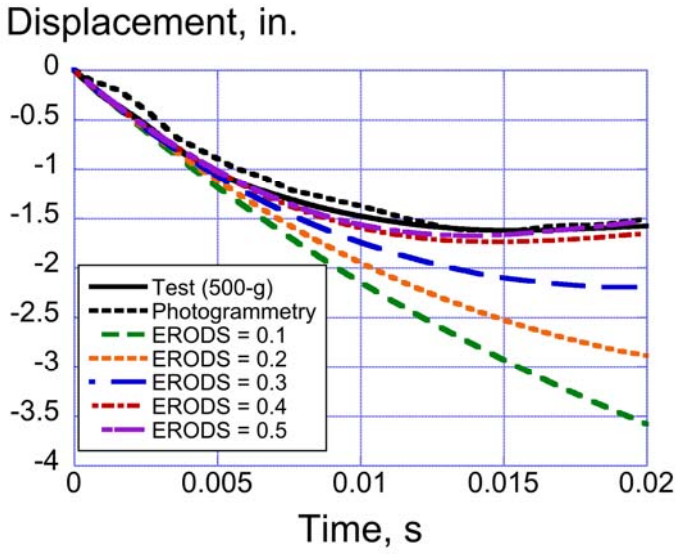

Figure 32. Mat 58 ERODS parameter study results for the cruciform section.

Discussion of Results

A variety of composite failure modes were evident during testing including brittle fracture, crushing of the material, ply delamination, layer splitting, and localized bending. The I-beam specimen exhibited uniform crushing of the material from the top edge that was aided by the presence of a crush initiator. Conversely, the T-section component exhibited delamination and localized brittle fracture, with very little crushing of the material. Likewise, the cruciform webs exhibited global buckling and crushing under impact loading. The ability to accurately model so many different structural deformation and composite failure modes is a major challenge for the current generation of nonlinear, explicit transient dynamic finite element codes.

Tests of the SARAP components were simulated using LS-DYNA shell-based finite element models. The shell elements were assigned either Mat 54 or Mat 58 material models to represent the behavior of the composite structure. In general, poor levels of correlation were seen when the Mat 54 model was used. The Mat 54 models tended to fail catastrophically in a brittle fashion, absorbing little kinetic energy.

All attempts to modify the Mat 54 material model to improve the crushing behavior failed, with one exception. An I-beam model was executed using Mat 54 properties, except that all failure strain inputs (DFAILM, DFAILS, DFAILT, and DFAILC) were undefined. The parameter EFS (Effective Failure Strain) was varied from 0.01 to 0.06 in increments of 0.01. The EFS parameter can be used instead of DFAILT, DFAILC, DFAILS and DFAILM. At each time step, LS-DYNA calculates an effective scalar strain for each integration point within an element and then compares the scalar strain to the EFS value. If the scalar strain is higher than EFS, then the integration point is deleted, regardless of loading condition. When all integration points have

failed, the element is removed. Thus, EFS controls element erosion/deletion, and does not represent progressive failure as is governed by Chang-Chang in Mat 54. Using Chang-Chang, the elastic properties of plies with the laminate stacking sequence are degraded as part of the ply-by-ply failure process. When all plies within an element are deleted, then the element is removed from the simulation.

Predicted acceleration-, velocity-, and displacement-time history responses are compared with test data in Figure 33 for the I-beam model executed with EFS=0.06. The impact velocity for this simulation was 189.6-in/s. This model was able to generate predicted responses that matched the test data reasonably well, especially when compared with the original Mat 54 results, shown in Figure 15. The experimental and predicted acceleration responses, shown in Figure 33(a), were filtered using a 1000-Hz Butterworth low-pass filter.

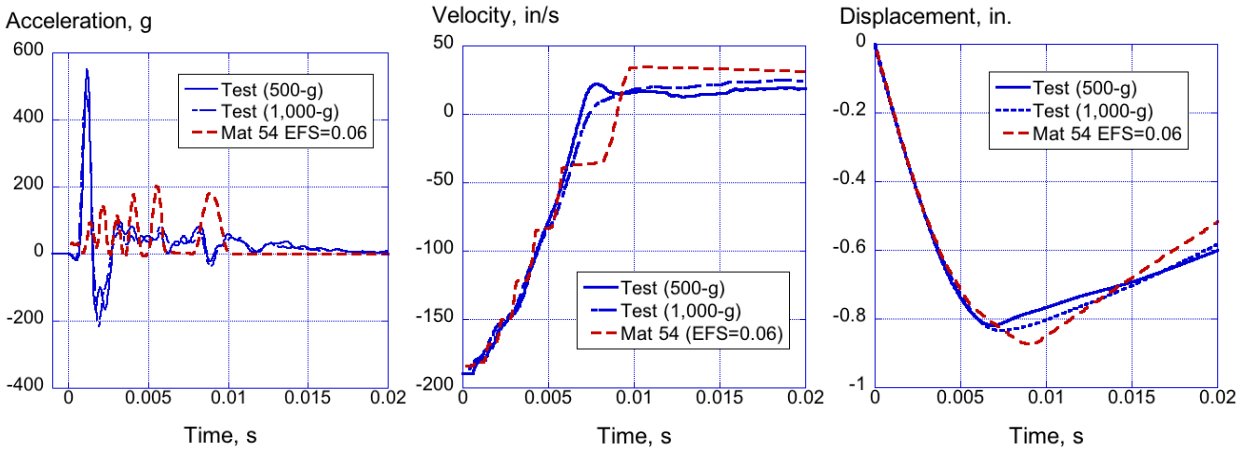

(a) Acceleration. (b) Velocity. (c) Displacement.

Figure 33. Experimental and Mat 54 analytical results for the I-beam 4-ft drop (velocity=189.6-in/s) with EFS=0.06.

However, despite the reasonably good comparison with time history responses, the predicted deformation, shown in Figure 34, does not match the test. The model begins to crush initially from the top edge. By 0.0064-s, elements have failed along the web-flange intersection almost completely separating these two parts on both sides. Also, a large "crack" has opened running from the middle of the top edge of the web to the side flange, which separates a large portion of the web from the specimen. By 0.024-s the failed portion of the web is removed from the model and no additional damage is seen. Conversely, the test article exhibits fairly uniform crushing of the specimen from the top edge, as shown in Figure 4.

Unlike Mat 54, Mat 58 incorporates parameters such as SLIMs and ERODS, which allow the analyst to incorporate some degree of plastic-like behavior into the model. For each of the component simulations, a parametric study was performed to evaluate the influence of ERODS. Results indicate that setting ERODS correctly is important in capturing the observed behavior. The ERODS parameter allows failed elements to carry small stresses, yet remain in the model. As seen when using Mat 54, once elements are removed from the simulation, holes are created in the model, resulting in stress concentrations. The model can quickly unzip and collapse. In general, the capability of LS-DYNA to accurately predict all of the composite failure modes is inconsistent. Material crushing of the I-beam components was successfully simulated; however,

debonding and delamination were not predicted. Current composite material models such as Mat 54 and Mat 55 are not capable of predicting delamination based on either fracture mechanics or energy–based approaches. However, if the location of a potential delamination or debond is known, the model could be modified to account for this failure mode using either tiebreak contact definitions or spot weld connections [17, 18].

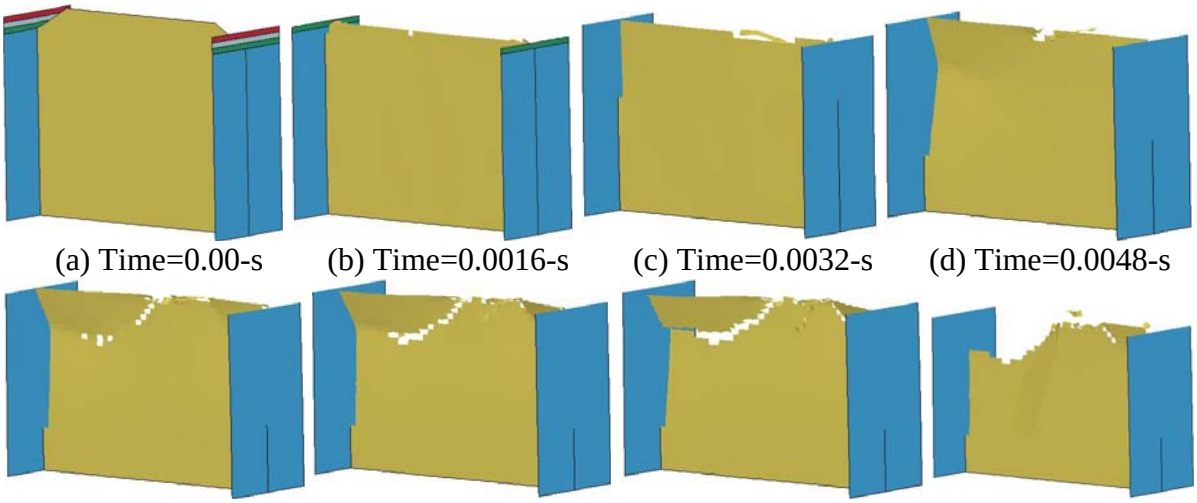

(a) Time=0.00-s (b) Time=0.0016-s (c) Time=0.0032-s (d) Time=0.0048-s

(e) Time=0.0064-s (f) Time=0.008-s (g) Time=0.0096-s (h) Time=0.024-s

Figure 34. Deformation pattern of I-beam model executed with Mat 54 (EFS=0.06).

Concluding Remarks

This report documents a research study to assess the capabilities of a nonlinear, explicit transient dynamic code, LS-DYNA, for predicting the impact response of composite airframe structures. Testing was conducted on components of varying complexity including I-beams, T-sections, and cruciform sections. All test articles were extracted from residual hardware of the Survivable Affordable Repairable Airframe Program (SARAP) Technology Validation Article (TVA), which was a prototype composite helicopter airframe manufactured primarily of thermoplastic graphite-epoxy unidirectional tape by Sikorsky Aircraft Corporation. Due to the varying complexity of the test articles, several different composite failure modes were evident during testing including brittle fracture, delamination, crushing of the material, and localized bending. In addition, structural failure modes occurred such as global buckling. The ability to accurately simulate so many different failure responses is a major challenge for the current generation of nonlinear, explicit transient dynamic finite element codes.

Finite element models were developed to represent the dynamic crush tests of I-beam, T-section, and cruciform components. Sikorsky Aircraft Corporation, the manufacturer of the SARAP hardware, provided most of the models to NASA as part of a cooperative research agreement. Once received, the models were updated and modified to best represent the test conditions. Simulations were conducted using LS-DYNA version 971 R6.0.0. The properties of the composite materials were represented using both a progressive in-plane damage model (Mat 54) and a continuum damage mechanics model (Mat 58) in LS-DYNA. Material properties for Mat 58 were determined by assessing literature data, evaluating existing material values provided by Sikorsky, and using a trial and error process in which laminated coupons were simulated under both tensile and compressive loading. Mat 54 properties were provided by Sikorsky.

In general, the Mat 54 simulations did a poor job in simulating the impact responses of the components. The Mat 54 models tended to fail catastrophically in a brittle fashion, absorbing little kinetic energy. Numerous parametric studies were conducted to find a set of parameters that would predict stable crushing, as opposed to brittle failure and structural collapse. None of these attempts were successful.

Unlike Mat 54, Mat 58 includes parameters, which allow the analyst to incorporate plastic-like behavior into the model. This feature allows failed elements to carry small stresses, yet remain in the model. As seen when using Mat 54, once elements are removed from the simulation, holes are created and stress concentrations are generated, leading to numerical instabilities and element failures. The model can quickly unzip and collapse. Mat 58 models of the I-beam were able to accurately predict material crushing. Likewise, Mat 58 models of the cruciform sections predicted global buckling behavior of the webs under dynamic loading. Consequently, excellent agreement was seen between the Mat 58 model predictions with the I-beam and cruciform responses.

However, during the impact test, the T-section failed primarily through delamination. Current composite material models such as Mat 54 and Mat 55 cannot predict delamination or debonding without *a priori* knowledge of where it will occur. If the location of a potential delamination or debond is known, the model can be modified to account for this failure mode using tiebreak contact or spot welds. Whether this is a reasonable or practical approach for modeling debonding or delamination was not evaluated in this study.

Because both Mat 54 and Mat 58 contain parameters that cannot be measured in the laboratory these parameters must be tuned through repeated test-analysis comparisons. Over time, an analyst may gain experience in selecting these parameters based on prior simulations. However, without relying on test data for comparison, it can be difficult to choose the correct values. As a result, these analysis methods cannot be considered truly predictive. However, it is fair to say that, while the capabilities of the current generation of explicit transient dynamic codes such as LS-DYNA may not provide accurate pre-test predictions of the impact response of composite airframe structures, the test response can be bounded using analysis.

Acknowledgements

The authors of this report gratefully acknowledge Charles Clarke, Brian Wilson, and Joseph Shen of Sikorsky, who helped establish the Space Act Agreement between NASA and Sikorsky, provided finite element models, and offered invaluable assistance in planning and executing the test and simulation program.

References

1. Carstensen T. A., Townsend W., and Goodworth A., “Development and Validation of a Virtual Prototype Airframe Design as Part of the Survivable Affordable Repairable Airframe Program,” Proceedings of the 64th American Helicopter Society Forum, Montreal, Canada, April 29-May 1, 2008.

2. Non-Reimbursable Space Act Agreement between Sikorsky Aircraft Corporation and NASA Langley Research Center for Collaborative Research Regarding Impact Testing and Simulation of Composite Airframe Structures, SAA1-1122, signed May 5, 2011.

3. Jackson K.E., Fuchs Y. T., and Kellas S., "Overview of the NASA Subsonic Rotary Wing Aeronautics Research Program in Rotorcraft Crashworthiness," ***Journal of Aerospace Engineering***, Special Issue on Ballistic Impact and Crashworthiness of Aerospace Structures, Volume 22, No. 3, July 2009, pp. 229-239.

4. Hallquist J. Q., "LS-DYNA® Keyword User's Manual," Volume I, Version 971, Livermore Software Technology Company, Livermore, CA, August 2006.

5. Hallquist J. Q., "LS-DYNA® Keyword User's Manual," Volume II Material Models, Version 971, Livermore Software Technology Company, Livermore, CA, August 2006.

6. Jackson K.E., Littell J.D., Horta L.G., Annett M.S., Fasanella E. L., Seal M.D., "Impact Testing and Simulation of Composite Airframe Structures," NASA Technical Memorandum, NASA-TM-2014-218169, February 2014.

7. Fasanella E. L., Littell J. D., Jackson K. E., and Seal M. D., "Simulating the Impact Response of Full-Scale Composite Airframe Structures," Proceedings of the 14th LS-DYNA® Users Conference, Dearborn, MI, June 3-5, 2014.

8. Chang, Fu-Kuo, and Chang, Kuo-Yen, "Post-Failure Analysis of Bolted Composite Joints in Tension or Shear-out Mode Failure Mode," ***Journal of Composite Materials***, Vol. 21, No. 9, September 1987, pp. 809-833.

9. Chang, Fu-Kuo, and Chang, Kuo-Yen, "A Progressive Damage Model for Laminated Composites Stress Concentrations," ***Journal of Composite Materials***, Vol. 21, No. 9, September 1987, pp. 834-855.

10. Tsai, S. W. and Wu, E. M., "A General Theory of Strength for Anisotropic Materials," ***Journal of Composite Materials***, Vol. 5, 1971, pp. 58–80.

11. Hahn H., and Tsai S.W., "Nonlinear Elastic Behavior of Unidirectional Composite Laminate," ***Journal of Composite Materials***, Vol. 7, 1973, pp. 102–110.

12. Hahn H., and Tsai S.W., "Nonlinear Behavior of Laminated Composites," ***Journal of Composite Materials***, Vol. 7, 1973, pp. 257–271.

13. Donadon M.V., de Almeida S.F.M., Arbelo M.A., and de Faria A.R., "A Three-Dimensional Ply Failure Model for Composite Structures, ***International Journal of Aerospace Engineering***, Vol. 2009, Article ID 486063, 2009.

14. Feraboli P., Wade B., Deleo F., Rassaian M., Byar A., "LS-DYNA MAT54 Modeling of the Axial Crushing of a Composite Tape Sinusoidal Specimen," ***Composites: Part A***, Vol. 42 (2011), pp. 1809-1825.

15. Matzenmiller A., Lubliner J., and Taylor R. L., "A Constitutive Model for Anisotropic Damage in Fiber Composites," ***Mechanics of Materials***, Vol. 20, 1995, pp. 125-152.

16. Xiao X., "Modeling Energy Absorption with a Damage Mechanics Based Composite Material Model," ***Journal of Composite Materials***, Vol. 43, No. 5, 2009, pp. 427-444.

17. Fleming, D. C., "Modeling Delamination Growth in Composites using MSC.Dytran," *Proceedings of the 2nd Worldwide Automotive Conference*, Dearborn, MI, Oct. 9-11, 2000.

18. Fleming D.C., Morrow C., Clarke C. W., Bird C. E., "Finite Element Simulation of Delamination with Application to Crashworthy Design," ***Journal of the American Helicopter Society***, Volume 53, Number 3, July 2008, pp. 267-281.